

A Microelectromechanical Systems-Based Vertical Magnetometer–Accelerometer with the Modulated Frequency Difference in One Microstructure

Ji-Man CHO*, Kyung Soo KIM¹, Sengdo AN¹, Choel Ho YEO², Kyoung SHIN²,
Byeong Kwon JU², Sang-Yong LEE, and Soo-Won KIM

ASIC Design Lab., Department of Electronics Engineering, University of Korea, Seoul 136 701, Korea

¹Navigation MEMS, R&D Center, Samsung Electromechanics Co., Suwon 442-743, Korea

²Display and Nano Devices Laboratory, College of Engineering, Korea University, Seoul 136-713, Korea

(Received October 1, 2007; accepted April 6, 2008; published online July 11, 2008)

This paper presents a vertical magnetometer–accelerometer capable of detecting simultaneously both the acceleration and the geomagnetic field. The conceived sensor detects the magnetic field by the Lorentz force and differentiates the magnetic field and the acceleration by the modulated frequency difference. The process uses a silicon-on-glass (SOG) wafer and the gold–silicon eutectic bonding for the wafer-level hermetic packaging. When the 10 mA current flows through the conductor, the measured resistances are an average of 10 Ω , so in total, 1 mW is consumed in the current driving element. When 35 μ T and 1 g is applied to the sensor at the same time, the fusion sensor has a sensitivity of 73 mV/g in acceleration sensing mode, and a sensitivity of approximately 1.63 mV/ μ T in magnetic field sensing mode. This newly developed sensor can be used in portable navigators that need a small size, low cost and low power electronic compass. [DOI: 10.1143/JJAP.47.5432]

KEYWORDS: MEMS, magnetometer–accelerometer, bulk-micromachining, Lorentz force, silicon-on-glass wafer, eutectic bonding

1. Introduction

The goal of this research is to develop electronic compass needed in cellular phones, portable navigators, and three-dimensional game devices. This electronic compass consists of a two-axis magnetometer to detect the platform orientation by geomagnetic reference and a two-axis accelerometer to compensate the tilt angle of the platform.¹⁾ With the additional z -axis accelerometer, the five axis sensors track down the three-dimensional motions of the game devices.

In a compass application, a magnetometer would need to be sufficiently sensitive to determine the direction of the magnetic field of the earth while simultaneously being sufficiently low power to be suitable for portable applications such as watches, cellular phones and portable navigators.²⁾ The flux gate magnetometers with an electroplated micro-coil and an inserted magnetic core have been developed by many groups, which can detect below the geomagnetic field.^{3–8)} However, since the electroplating is not compatible with the silicon accelerometer fabrication, the silicon accelerometers and the flux-gate magnetometers should be fabricated separately and assembled in the final board. Further, several groups have reported the Lorentz force based resonant type magnetometer, whose process is the complementary metal oxide semiconductor (CMOS)-compatible, high resolution, and low power consumption.^{9–13)} However, since the resonant structure is easily affected by external acceleration, they are disadvantageous in that an external acceleration causes interference in the magnetic signal channel. In this paper, we have reported the Microelectromechanical systems (MEMS)-based magnetometer–accelerometer capable of detecting simultaneously both the magnetic field and the acceleration with the minimum interferences. The conceived sensor detects the magnetic field by the Lorentz force in the conducting film and differentiates the magnetic field and the acceleration by the modulated frequency difference. This method can

integrate the needed x -axis magnetometer and z -axis accelerometer in one silicon chip with one batch process and thus the assembly process is simplified and the total size of the navigation compass system can be reduced.

2. Operational Principle and Design Concept

A schematic of the conceived magnetometer–accelerometer is presented in Fig. 1. The microstructure design is based on the Lorentz force arising from a current-carrying conductor in the magnetic field.¹³⁾ To realize this concept, a gold film is evaporated on the spring of a silicon accelerometer and an upper sensing electrode is formed on the upper cap wafer. A movable silicon mass plate is suspended over a glass substrate by means of L-shape springs, which are designed to be more easily movable in the z -direction, whereas the suspensions in the x - and y -directions are significantly stiffer. As a result, the Lorentz force or the acceleration vertically displaces the suspended mass plate and thus upper sensing electrode detects the acceleration in the perpendicular direction and the magnetic field in the parallel direction to the substrate as shown in Fig. 1(b). When the current is applied to the input electrode, the current flows from the input electrode into the gold thin film on the two springs, and finally reaches to the ground electrode. If an ac current of frequency equal to the beam's resonant frequency is applied to flow along the conductor beam, the Lorentz force in the x - or y -axis magnetic field is given by the following:

$$F_L = Il \sin(\omega_l t) B, \quad (1)$$

where F_L is the Lorentz force into the z -direction, l is the gold conductor path length, I is the current through the spring, ω_l is the angular frequency of the current, and B is the magnetic flux density in the x - or y -axis directions. Because the Lorentz force is proportional to both the magnetic flux density and the electrical current, the same deflection takes place if the magnetic field is reduced and the current is increased by the same factor. When ω_l is tuned to the structure resonant frequency, the z -axis displacement is

*E-mail address: microjm@korea.ac.kr

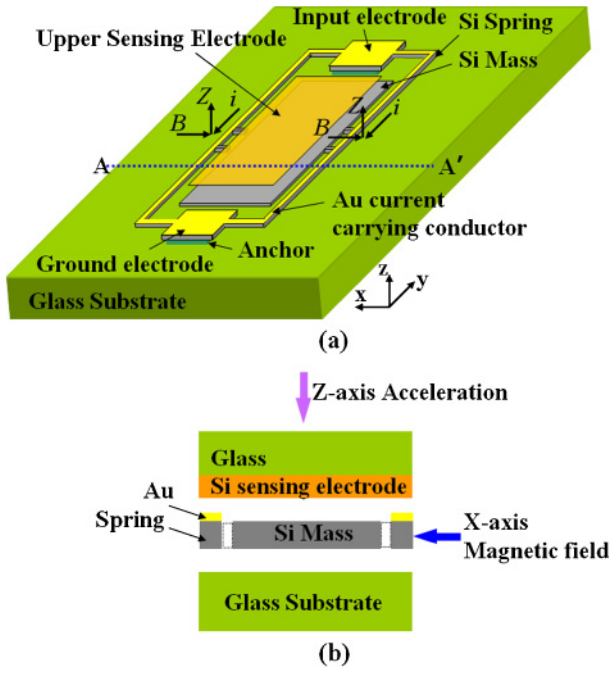


Fig. 1. (Color online) Schematic view of (a) the proposed vertical magnetometer-accelerometer and (b) cross section of line A–A' (B : magnetic field, Z : displacement, i : current).

$$Z_B = \frac{IB}{k} Q \sin(\omega t - \phi), \quad (2)$$

where Z_B is the displacement in the z -direction due to the Lorentz force, k is the spring stiffness in the z -direction, Q is the mechanical quality factor, and ϕ is the phase difference. From this equation, it can be seen that this motion (Z_B) is a modulated form of the current and the magnetic field amplitude and the motion amplitude is linearly proportional to the drive current (I), the magnetic field (B), and the mechanical Q -factor.

If the z -axis acceleration is applied to the sensor, the z -axis displacement is described as follows:

$$Z_A = \frac{ma}{k}, \quad (3)$$

where Z_A is the displacement in the z -axis direction due to the acceleration, m is the mass, and a is the acceleration. Since Z_A is not a modulated form with current frequency, Z_A and Z_B are far away in the frequency domain spectrum and can be separated into each component with a suitable frequency filter. The vertical displacement of the mass plate is converted into a capacitance change of planar capacitors, which consist of the movable mass and the upper sensing electrode. Consequently, both magnetic field and acceleration are detected from capacitance change and separated into each signal by the modulated frequency difference in one microstructure.

The sensor design needs to be optimized for large sensitivity in order to detect the weak geomagnetic field of $35 \mu\text{T}$ and acceleration of $1g$ ($= 9.8 \text{ m/s}^2$). The designed spring structure has a thickness of $10 \mu\text{m}$, a width of $20 \mu\text{m}$, and a length of $1900 \mu\text{m}$. The height of the spring is given by the silicon device layer of the silicon-on-glass (SOG) wafer while the length and width are limited by the stress gradient in the gold–silicon and the available design area. The spring

Table I. The design parameters (calculated value).

Silicon spring thickness (μm)	10
Silicon spring width (μm)	20
Silicon spring length (μm)	1900
Gold path thickness (μm)	0.25
Gold path width (μm)	18
Sensing gap (μm)	0.25
Mass plate area (μm^2)	400×2000
Structure mass (μg)	15.38
Spring stiffness (N/m)	3.55
Resonant frequency (kHz)	1.325

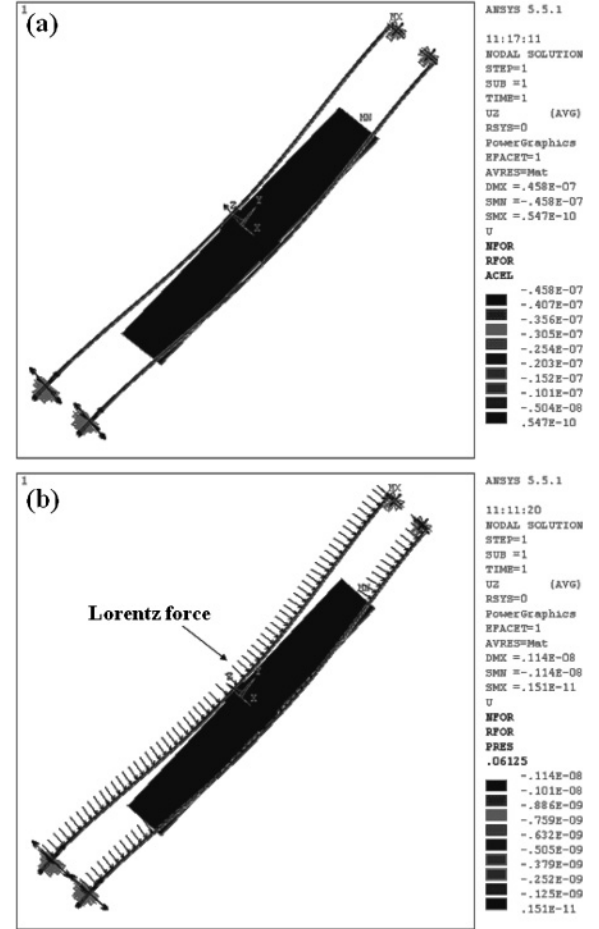


Fig. 2. ANSYS FE simulation results: (a) deflection due to the acceleration of $1g$ and (b) deflection due to the Lorentz force at a geomagnetic field of $35 \mu\text{T}$.

stiffness and resonant frequency have been calculated using an analytical model.¹⁴⁾ The design parameters and the calculated values are presented in Table I. The calculated spring stiffness and resonant frequency are 3.55 N/m and 1.325 kHz , respectively. By combining movable masses and upper sensing electrodes, the capacitor yields an initial sense capacitance of approximately 3.2 pF by design at a gap of $d = 0.25 \mu\text{m}$. The finite element program ANSYS is used to do the mechanical modeling for the more accurate analysis. Figure 2 shows the simulation results of the maximum displacement in the case that either the acceleration of $1g$ input to the whole structure or the Lorentz force input onto the surface of the spring. The maximum current i

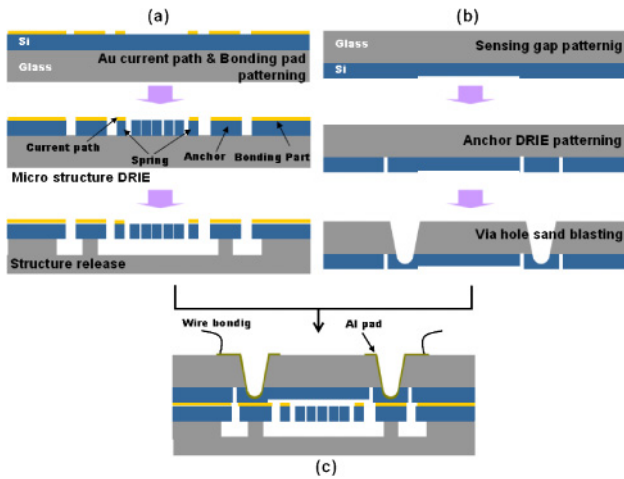


Fig. 3. (Color online) Fabrication process: (a) microstructure process, (b) sensing cap process, and (c) wafer level packaging process.

is determined by both the geometry of the spring and the conductivity of the gold, and a typical value used here is 10 mA. If the quality-factor of 10 and 10 mA current are assumed, a displacement of 1.14 nm/T and 45.8 nm/g is simulated, respectively. Although the ratio of Z_A/Z_B is 40, each motion can be separated with minimum interferences by using the frequency difference.

3. Fabrication

The total fabrication process consists of three main steps as shown in Fig. 3 and sensor fabrication is based on a six-mask, two-wafer silicon bulk-micromachining process. In this report, we introduce the SOG wafer because far fewer fabrication steps are needed and the surface on which the sensor is fabricated is smoother. In the micro structure process [Fig. 3(a)], the starting material, SOG wafer is prepared by anodically bonding the (100) silicon wafer to the glass wafer (Pyrex 7740, 400 μm) and then the 10 μm thick silicon device layer is accomplished by chemical mechanical polishing (CMP). The fabrication process starts with the deposition of a Cr (30 nm)/Au (0.25 μm) layer on the SOG substrate. Then, the gold is patterned with lift-off techniques using an image reversal photoresist (Micro-Chemicals TI 35ES), and acts as a current carrying conductor and eutectic bonding pad. The gold layer survives the following HF wet etching process. The vibrating mass and the spring are patterned using conventional positive photoresist and etched with the inductively coupled plasma reactive ion etching (ICP RIE; STS) and are released by the 4-min HF glass wet etching and the subsequent drying after dipping 3 min in isopropyl alcohol solution. In the cap wafer process [Fig. 3(b)], the cap wafer is an inverted SOG, which is composed of the (100) silicon wafer (100 μm) and the glass wafer (Pyrex 7740, 300 μm). The silicon is patterned and etched by the RIE for 20 s to make the shallow sensing gap with a depth of 0.25 μm and then the corresponding anchors are formed by the deep RIE process. Finally, the via holes for feed-through are formed by sand-blasting process. In the final wafer-level packaging process [Fig. 3(c)], the gold on anchors in the structure SOG wafer is bonded with the silicon anchors in cap SOG wafer at 450 $^{\circ}\text{C}$ and 760 Torr

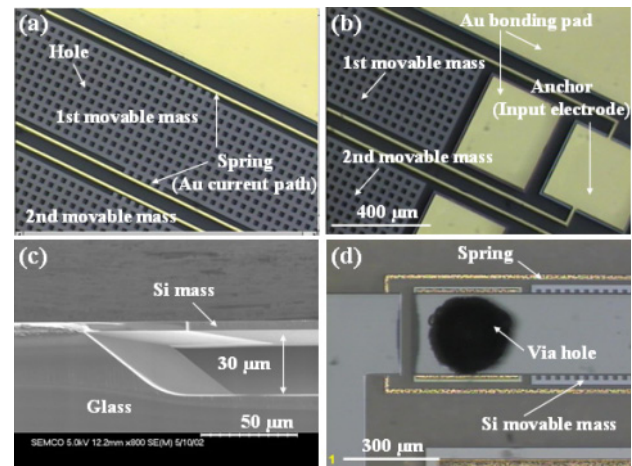


Fig. 4. (Color online) Photomicrograph of (a, b) the fabricated microstructure, (c) the cross-section of the released microstructure on the SOG wafer, and (d) the eutectic bonded chip, respectively.

with tool pressure of 1 bar for 30 min. After patterning of aluminum for wire bonding, the chip is diced and wire-bonded to the testing board.

Figures 4(a) and 4(b) represents the closed view of two positions of microstructure fabricated on SOG wafer. The photomicrograph displays the anchor structure, etch holes, gold current path, gold eutectic bonding pad, and electrodes. A large number of holes perforate the mass plate in order to minimize weight of the movable mass and simultaneously achieve high mechanical rigidity. As can also be seen, the deposited gold layer acts as current carrying conductor and eutectic bonding pad. In order to reduce the electrical resistance, a thin layer of the gold is formed on the spring beam. Since a larger current can flow through the conductor at a given voltage, the sensor can detect a very small signal as the geomagnetic field as a function of increasing the evaporated gold thickness. However, the continuous increasing of the gold thickness may deteriorate sensitivity in accordance with the increase of spring stiffness in the z -direction. In this study, we have selected the gold thin film with a thickness of 0.25 μm . Besides, the beam structure may be deformed by an internal stress gradient or even by thermal effects coming from the fabrication process. All of these effects can cause disparity of the sensor performances and degradation of the fabrication yield. When the 10 mA current flows through the conductor, the measured resistances are an average of 10 Ω , so in total, 1 mW is consumed in the current driving element of the magnetometer–accelerometer. Figure 4(c) shows the cross-section of microstructure released by HF glass wet etching. The weak vibrating structure is easily released without any sticking problem because of the large separation gap ($\sim 30 \mu\text{m}$) between the movable mass and the etched glass surface. Accordingly, this SOG wafer based process can be effectively applied to enhance the device yield in MEMS production. Figure 4(d) shows the sectional top view of the eutectic bonded chip. If the sensor is operated in vacuum at its mechanical resonance, the z -axis motion amplitude scales with the quality factor, Q .¹⁵⁾ The improvement of the sensor resolution should thus be achievable using a vacuum package. However, the high vacuum encapsulation causes

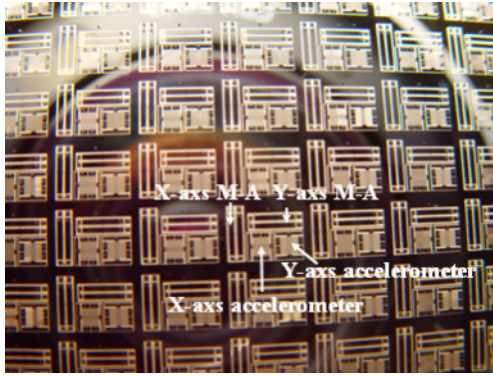


Fig. 5. (Color online) Perspective view of the wafer-level packaged chip arrays using the eutectic bonding (M-A: magnetometer-accelerometer).

the problems such as the deterioration of shock reliability and difficulty of reproducibility of wafer level packaging. Besides, since the high vacuum encapsulation of the sensors is sensitive to the small variation of pressure and temperature, an additional calibration is necessary. Therefore, in this work the gold-silicon eutectic bonding has been done at 1 atmospheric condition in order to realize the low vacuum state in the wafer level packaged chip.

Figure 5 represents the perspective view of the wafer-level packaged chip array. As shown, The four sensors are formed on the same substrate and the overall dimensions of the five-axis sensor are approximately 5.8 mm (w) \times 4.45 mm (l) \times 0.85 mm (t). To measure the *x*- and *y*-axis magnetic field, the two vertical magnetometer-accelerometers are perpendicularly aligned. Also, for compensating the *x*- and *y*-axis tilt of the platform, the two conventional accelerometers are perpendicularly aligned. Since the vertical magnetometer-accelerometer is capable of detecting both the magnetic field and accelerometer, the four sensors fabricated on the same chip can realize the five-axis sensor. Therefore, in the case that the magnetometer-accelerometer is employed in a navigation system, the assembly process is simplified and the total size of the navigation compass system can be reduced. In addition, in comparison with hybrid microsystems, this one-batch process approach can avoid additional noise inputs generated by multi-substrate bonding.

4. Measurements

4.1 Electronic circuit and modulation scheme

Figure 6 shows the circuit diagram of applying the main carrier and the driving current. In order to drive the sensor, a main carrier ($0.3 V_{pp}$) is applied to the mass and an ac current ($1 V_{pp}$), which is set to the structure resonant frequency flows through the conductor. Therefore, the main carrier voltage is set to the same level and the current-driving voltage is set to the different levels so that the former drives no current and the latter drives the current. As mentioned above, gap variation yields a capacitance change of capacitors formed by movable mass and upper sensing electrode and charge amplifier for capacitor convert the capacitance into electrical voltage.

In this study, we have proposed the novel scheme measuring each signal simultaneously, minimizing the interference between the magnetic signal and the accel-

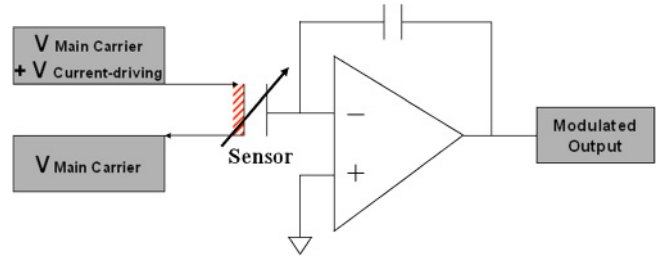


Fig. 6. (Color online) Schematic of circuit for driving and sensing.

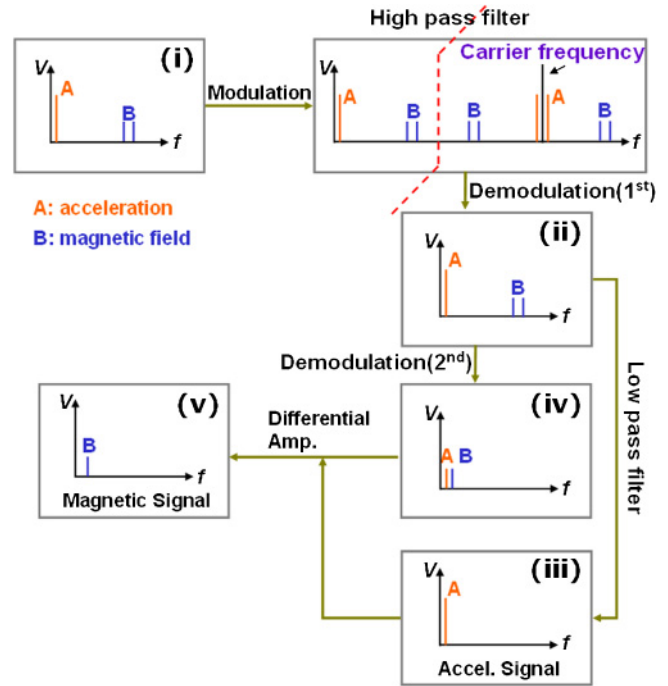


Fig. 7. (Color online) Schematic of novel scheme measuring signal with minimum interference.

eration signal, as shown in Fig. 7.¹⁶⁾ First, the ac current frequency (B) is far away from the acceleration frequency (A). From eqs. (2) and (3), we can know that the magnetic field is modulated with the ac resonating current but the acceleration can not be modulated with current. As shown in Fig. 6, the main carrier voltage drives no current and the ac current driving voltage drives the current. Therefore, the acceleration is modulated with the main carrier frequency and the magnetic field signal is modulated with the ac current frequency. Since the applied acceleration frequency is typically less than 100 Hz and the magnetic field signal is modulated with the current resonating frequency (about 1 kHz), in an ideal case there is no interference between them. After the first demodulation with the main carrier signal, the acceleration signal and the ac current modulated magnetic signal are recovered (ii). The end signal of acceleration is obtained by low pass filtering (iii). The recovered magnetic field signal modulated with the ac current signal is again demodulated with the current-driving signal (iv) and a final magnetic field signal is recovered (v). But the magnetic field signal has an undesirably added acceleration signal because of the sensing gap changes with acceleration and interference between the ac current and the

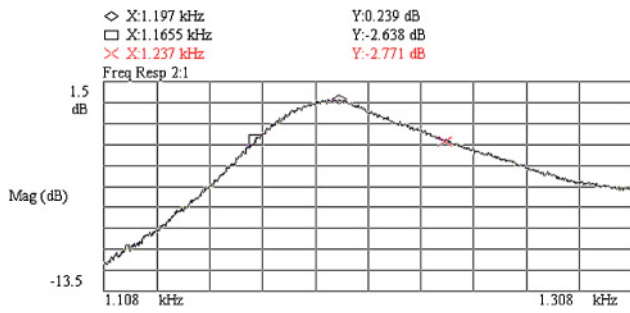


Fig. 8. (Color online) Plot of structure resonant characteristics.

main carrier (iv). Thus, the first demodulated acceleration signal (iii) is subtracted from the magnetic field signal (iv).

4.2 Performance test

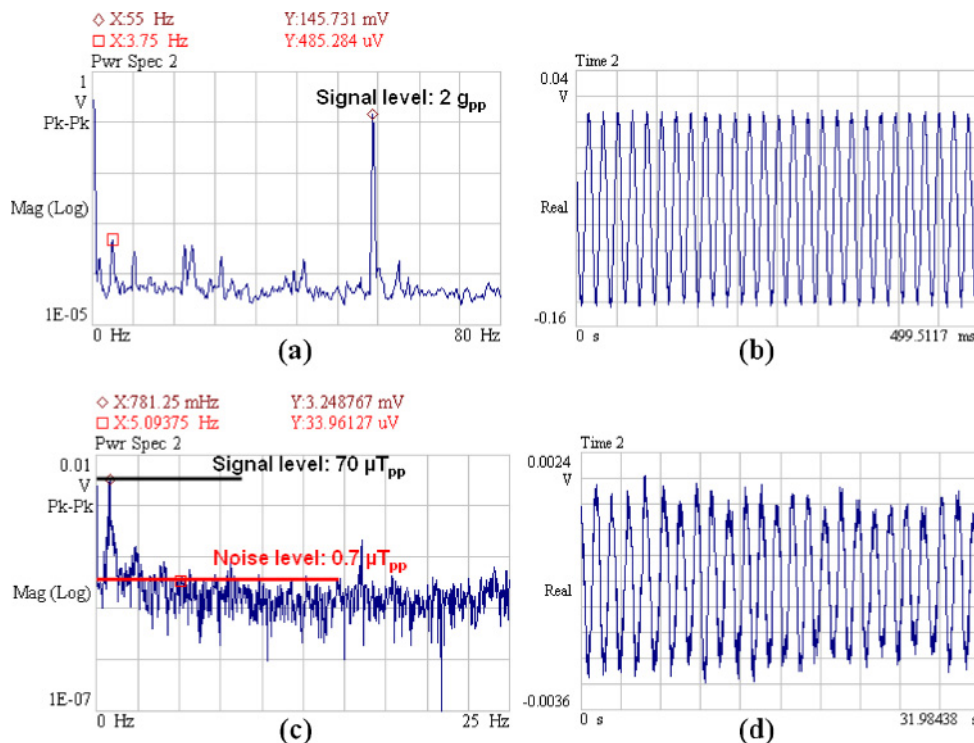
Figure 8 shows the resonant characteristics of the sensor. To measure the quality factor and resonant frequency, the frequency of excitation is swept until the amplitude signal is maximized and the resonant characteristic is monitored by a spectrum analyzer (HP4194A). In this measurement, the sensor is oriented to maximize the Lorentz force, arising from the interaction between the geomagnetic field (approximately $35 \mu\text{T}$) and the ac current in the conducting path. From recording gain-phase plots and the resonance bandwidth formula, both the resonant frequency and the quality factor can be derived.¹²⁾ The measured resonant frequency is 1.197 kHz and the measured Q -value is approximately 17. The difference between the measured and the calculated value of resonant frequency could be attributed to the deep RIE process variations which effect on the spring constant. Besides, the measured low Q -value indicates that there is another structural damping in addition to viscous damping.

This structural damping could be due to the gold layer that brings the current onto the spring beam.

The geomagnetic field and acceleration measurements are found through experiment and the test results are shown in Fig. 9. To measure the sensitivity of accelerometer, the acceleration of $2.0g_{\text{pp}}$ (peak-to-peak) at 55 Hz is applied to the sensor in the z -direction by a vibrating shaker. As shown in Fig. 9(a), the applied acceleration yields an incremental output of 145.73 mV and the noise equivalent acceleration is $1.65 \times 10^{-3} g_{\text{pp}}$, which is equivalent to the tilt angle of $0.16 \text{ deg}_{\text{pp}}$. Figure 9(b) shows the time domain signal of Fig. 9(a).

Figure 9(c) shows the measured sensitivity when only the magnetic field of $70 \mu\text{T}_{\text{pp}}$ (north-to-south) corresponding to the geomagnetic field is applied in the x -direction to the sensor. And Fig. 9(d) shows the time domain of the measured magnetic signal. Even small incremental magnetic fields of $70 \mu\text{T}_{\text{pp}}$ yield an incremental output of 3.25 mV, which is easily resolved by resonant detection electronics. The noise equivalent magnetic field is $0.7 \mu\text{T}_{\text{pp}}$, which is equivalent to a $1 \text{ deg}_{\text{pp}}$ orientation by the geomagnetic reference. Further optimizations in electronic modules and sensor design should allow the precision measurements of magnetic field in the region below the magnitude of the geomagnetic field. The measured sensitivity in acceleration intensity is about 45 times larger than that in the magnetic flux density and this result is well consistent with the simulation results of maximum deflection as presented in Fig. 2.

To investigate the interference between the magnetic field signal and the acceleration signal, both the acceleration and the geomagnetic field are applied to the sensor at the same time. Figure 10 shows the magnetic field signal channel when there is the static magnetic field of $70 \mu\text{T}_{\text{pp}}$ and the

Fig. 9. (Color online) Test results of (a, b) acceleration signal of $2.0g_{\text{pp}}$ and (c, d) magnetic field signal of $70 \mu\text{T}_{\text{pp}}$.

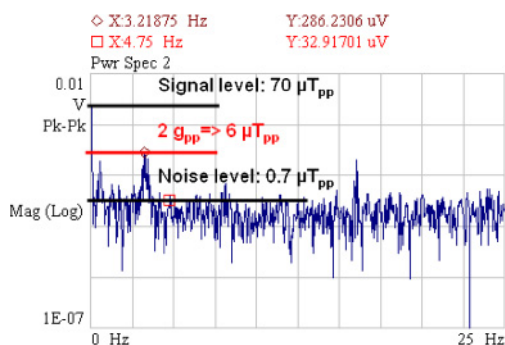


Fig. 10. (Color online) Test results of acceleration $2.0g_{pp}$ interference in the magnetic field signal channel.

acceleration of $2.0g_{pp}$ at about 3 Hz. Signal level of acceleration diminishes dramatically from 145.73 mV to 286.23 μ V by the modulation frequency difference of Fig. 7 and finally, there is about 8.8% ($= 6\mu T_{pp}$) interference of $2.0g_{pp}$ acceleration in the $70\mu T_{pp}$ magnetic field range. This undesirably added acceleration signal could be caused by the sensing gap changes with acceleration and interference between the ac current and the main carrier. From the results, we can see that the newly conceived scheme detecting simultaneously both the acceleration and the geomagnetic field is successful with minimum interference to each other.

5. Conclusions

In this paper, a new type of magnetometer–accelerometer having dual sensing function is designed, fabricated and tested. Both magnetic field and acceleration are simultaneously detected and separated into each signal by the modulated frequency difference in one microstructure. The sensor is fabricated with an SOG bulk-micromachining

process and hermetically packaged by the eutectic bonding. Performance test shows enough minimum equivalent noise level of acceleration and magnetic field and interferences for electronic compass. With the initial version of this sensor and the additional acceleration sensors, the five-axis sensors are constituted and can function as an electronic compass in the portable navigator.

- 1) J. C. Michael: Honeywell SSEC [www.magneticsensors.com/magnetic/datasheets].
- 2) J. Lenz and A. S. Edelstein: *IEEE Sens. J.* **6** (2006) 631.
- 3) E. Belly, S. E. Gilbert, O. Dezuari, M. Sancho, and M. A. M. Gijis: *Sens. Actuators A* **85** (2000) 304.
- 4) T. M. Liakopoulos and C. H. Ahn: *Sens. Actuators A* **77** (1999) 66.
- 5) R. Gottfried-Gottfried, W. Budde, R. Jahne, H. Kuck, B. Sauer, S. Ulbricht, and U. Wende: *Sens. Actuators A* **54** (1996) 443.
- 6) P. Kejik, L. Chiesi, B. Janossy, and R. S. Popovic: *Sens. Actuators A* **81** (2000) 180.
- 7) L. Chiesi, P. Kejik, B. Janossy, and R. S. Popovic: *Sens. Actuators A* **82** (2000) 174.
- 8) H. Gruger and R. Gottfried-Gottfried: *Sens. Actuators A* **91** (2001) 61.
- 9) R. B. Givens, J. C. Murphy, R. Osiander, T. J. Kistenmacher, and D. K. Wickenden: *Appl. Phys. Lett.* **69** (1996) 2755.
- 10) Z. Kadar, A. Bossche, P. M. Sarro, and J. R. Mollinger: *Sens. Actuators A* **70** (1998) 225.
- 11) R. B. Givens, D. K. Wickenden, D. A. Oursler, R. Osiander, J. L. Champion, and T. J. Kistenmacher: *Appl. Phys. Lett.* **74** (1999) 1472.
- 12) H. Emmerich and M. Schöfthaler: *IEEE Trans. Electron Devices* **47** (2000) 972.
- 13) D. K. Wickenden, J. L. Champion, R. Osiander, R. B. Givens, J. L. Lamb, J. A. Miragliotta, D. A. Oursler, and T. J. Kistenmacher: *Acta Astron.* **52** (2003) 421.
- 14) S. D. Senturia: *Microsystem Design* (Kluwer, Boston, MA, 2000) p. 202.
- 15) B. Eyre, K. S. J. Pister, and W. Kaiser: *IEEE Electron Device Lett.* **19** (1998) 496.
- 16) J.-M. Cho, K. S. Kim, S. An, S.-Y. Lee, and S. W. Kim: *Electrochem. Solid-State Lett.* **10** (2007) J108.